JOURNAL OF THE ROYAL SOCIETY Interface

J. R. Soc. Interface (2012) **9**, 1908–1924
doi:10.1098/rsif.2011.0841
Published online 1 February 2012

Hydrodynamics of the double-wave structure of insect spermatozoa flagella

On Shun Pak, Saverio E. Spagnolie and Eric Lauga*

Department of Mechanical and Aerospace Engineering, University of California San Diego, 9500 Gilman Drive, La Jolla, CA 92093-0411, USA

In addition to conventional planar and helical flagellar waves, insect sperm flagella have also been observed to display a double-wave structure characterized by the presence of two superimposed helical waves. In this paper, we present a hydrodynamic investigation of the locomotion of insect spermatozoa exhibiting the double-wave structure, idealized here as superhelical waves. Resolving the hydrodynamic interactions with a non-local slender body theory, we predict the swimming kinematics of these superhelical swimmers based on experimentally collected geometric and kinematic data. Our consideration provides insight into the relative contributions of the major and minor helical waves to swimming; namely, propulsion is owing primarily to the minor wave, with negligible contribution from the major wave. We also explore the dependence of the propulsion speed on geometric and kinematic parameters, revealing counterintuitive results, particularly for the case when the minor and major helical structures are of opposite chirality.

Keywords: swimming micro-organisms; flagellar hydrodynamics; insect sperm motility

1. INTRODUCTION

Locomotion in fluids is ubiquitous in nature, with examples spanning a wide range in size from bacterial motility to the swimming of whales. It plays fundamental roles throughout the lives of animals in such endeavours as predation and finding a mate for reproduction [1]. Lying along the interface between biology and fluid dynamics, biological locomotion at small scales has received substantial attention from biologists and engineers in recent years [2,3].

The physics governing locomotion in fluids is very different for microscopic organisms (e.g. bacteria, spermatozoa) and macroscopic organisms (e.g. fishes, humans). The dramatic difference is because of the competition between inertial and viscous effects in the fluid medium. The Reynolds number, $Re = UL/\nu$ (with U and L characteristic velocity and length scales, and ν the kinematic viscosity) is a dimensionless parameter that measures the relative importance of the inertial forces to viscous forces in a fluid. Locomotion of larger animals in fluids takes place at moderate to large Reynolds numbers, where inertial forces dominate. At this scale, swimming and flying are generally accomplished by imparting momentum into the fluid opposite to the direction of locomotion. Micro-organisms meanwhile inhabit in a world of low Reynolds numbers, where inertia plays a negligible role and viscous damping is paramount. The Reynolds number ranges from 10^{-6} for bacteria to 10^{-2} for spermatozoa [4]. The absence of inertia imposes stringent constraints on a micro-organism's locomotive capabilities.

Many micro-organisms propel themselves by propagating travelling waves along one or many slender flagella [4]. The motility features of these flagella depend on the cell type, either prokaryotic (cells without a nucleus) or eukaryotic (cells with nuclei). The flagella of prokaryotic bacteria, such as those used by *Escherichia coli*, are helical in shape and are passively rotated at their base by a motor embedded in the cell wall. The rotation propagates an apparent helical wave from the sperm head to the distal end of the flagellum, propelling the cell in the opposite direction. Eukaryotic flagella exhibit a different internal structure, called an axoneme, which is composed of microtubules, proteins and protein complexes such as dynein molecular motors. The dynein arms convert chemical energy contained in adenosine triphosphate into mechanical energy, inducing active relative sliding between the microtubules, which in turn leads to bending deformations that propagate along the flagellum. A common structure of the axoneme has a ring of nine microtubule doublets spaced around the circumference and two additional central microtubules (the so-called $9 + 2$ axoneme). Other variations of the axonemal structure have also been observed [5].

Generally, three levels of complexity in undulatory beat patterns are observed in eukaryotic flagella [5,6], following a hierarchy in the structure of the axoneme: (i) the lowest in the hierarchy is a simple planar beating pattern, as in human and sea-urchin spermatozoa flagella (figure 1*a*), with the common $9 + 2$ axoneme structure; (ii) a more complicated three-dimensional

*Author for correspondence (elauga@ucsd.edu).

Received 1 December 2011
Accepted 4 January 2012

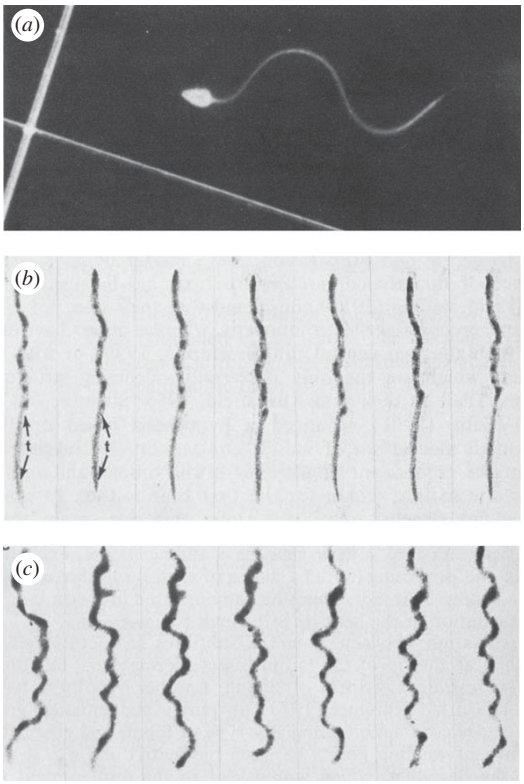

Figure 1. A hierarchy of the complexity of flagellar beating pattern observed in eukaryotic cells. (*a*) Planar-wave pattern in sea-urchin spermatozoa flagella [7]; (*b*) helical-wave pattern in *Gryllotalpa gryllotalpa* [6]; and (*c*) double-wave pattern in *Haematopinus suis* [6]. All images were reproduced with permission: (*a*) from Rikmenspoel & Isles [7]. Copyright 1985 Elsevier; (*b*,*c*) from Baccetti [6]. Copyright 1972 Elsevier.

helical beating pattern is exhibited by some insect spermatozoa with a $9 + 9 + 2$ axoneme, as in *Gryllotalpa gryllotalpa* (figure 1*b*); and (iii) the highest level of complexity is a double-wave pattern observed in some insect spermatozoa with a $9 + 9 + 2$ axoneme and accessory bodies endowed with ATPase activity, as in *Haematopinus suis* (figure 1*c*). A vast diversity in sperm structure is found in insects [8], and the hierarchy described is also observed even just within the realm of insect spermatozoa flagella [5,6]. Figure 2 shows a schematic of a pterygote insect flagellosperm and its ultrastructure (reproduced with permission from Werner & Simmons [5]). Similar to the $9 + 2$ axoneme observed in cilia and flagella of many plant and animal cells, the central core of the insect sperm axoneme is composed of two central microtubules surrounded by a ring of nine microtubule doublets. However, the ring of nine microtubule doublets is surrounded by another nine accessory tubules, forming the characteristic $9 + 9 + 2$ arrangement of the insect sperm axoneme. In addition to the more complicated microtubule arrangement, two prominent features of inset spermatozoa flagella are the mitochondrial derivatives and accessory bodies running along the axoneme (see the study of Werner & Simmons [5] for a thorough review of insect sperm structure).

Although the structure of many different spermatozoa has been examined, the rapid and divergent evolution in sperm morphology is not well understood [5,9]. Hydrodynamic considerations of the relationship between flagellar morphology and functional parameters such as the swimming speed may provide useful information for explaining the evolutionary divergence. Because of its intricate nature, the double-wave structure is less well-explored than wave types sitting lower in the hierarchy. Relevant studies on the planar and helical wave structures are abundant and well-developed (see the classical and recent reviews [2–4]), but we are not aware of any hydrodynamic studies dedicated to the double-wave structure. Here, we present a hydrodynamic study on the motility of insect spermatozoa exhibiting a double-wave beat pattern.

The double-wave pattern is characterized by the simultaneous presence of two kinds of waves—a minor wave with small amplitude and high frequency superimposed on a major helical wave of large amplitude and low frequency. The minor wave has also been observed to be approximately helical [10], and the combined activity of the two is described as a double-helical beating pattern [5]. The double-wave structure was first observed in *Tenebrio molitor* and *Bacillus rossius* by Baccetti *et al.* [11,12], and was also later found in *Lygaeus* [13], *Culicoides melleus* [14], *Aedes notoscriptus* [15], *Ceratitis capitata* [16], *Drosophila obscura* [17], *Megaselia scalaris* [18], and more recently in *Aleochara curtula* [10] and *Drusilla canaliculata* [19]. Figure 3 compiles a collection of images of spermatozoa exhibiting the double-wave structure. Werner & Simmons [5] have presented a thorough review of this complex structure in insect spermatozoa.

Most studies on insect spermatozoa focus on the sperm ultrastructure, there are very few studies on insect sperm motility [5]. Many important geometric and kinematic data required for hydrodynamic modelling of the double-wave structure are unavailable. In particular, we are not aware of any information about the chirality of the minor helical structure relative to the major helical structure. The generation and propagation mechanism of the double-wave is also not yet fully understood. Baccetti *et al.* [11,12] have suggested that the accessory bodies and the axoneme are responsible for the major and minor waves, respectively, whereas Swan [15] has stated that the major wave may be owing to the sliding of the accessory tubule against the axonemal doublets. More recently, Werner *et al.* [10] have proposed a completely different line of thought, suggesting that the major wave is not in act a real wave but a static helical structure formed owing to the coupling of static forces of the axoneme, mitochondrial derivatives and plasma membrane. The apparent propagation of the major wave could be owing to the passive rolling of the entire cell and might in fact be mistaken for an active, propagating wave under the microscope. It has therefore been suggested that the sperm motility is caused solely by the minor wave. The relative extent of the contribution of the major and minor waves to propulsion is thus still an open question [14]. With the hydrodynamic study presented in this paper, we hope to provide physical insights on these unresolved problems.

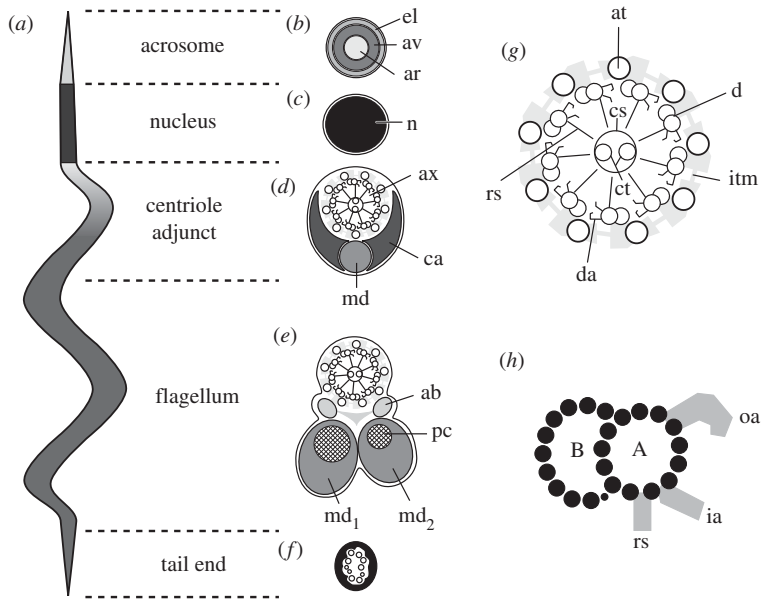

Figure 2. Schematic of the ground plan of a pterygote insect flagellosperm and its ultrastructure. (*a*) A typical filiform insect spermatozoon. Although not easily visible from the outside, it can be divided into five distinct parts: acrosome, nucleus, centriole adjunct, flagellum, and tail end. (*b*) Cross section of the acrosome showing its trilayered arrangement of an inner acrosomal rod (ar), an acrosomal vesicle (av) and an outer extra acrosomal layer (el). (*c*) Cross section of the nucleus (n) showing condensed chromatin. (*d*) Cross section of the posterior centriole adjunct region. This part of the spermatozoon is characterized by the electron-dense centriole adjunct material (ca), often surrounding the anterior part of the axoneme (ax) and the tip of one of the mitochondrial derivatives (md). (*e*) Cross section through a representative segment of the flagellum. In addition to the axoneme, two accessory bodies (ab) and the two mitochondrial derivatives of often different size (md1, md2) can be seen. The mitochondrial derivatives typically bear paracrystalline inclusions (pc). (*f*) Cross section through the tail end showing dissociated axonemal tubules. (*g*) Cross-sectional representation of a typical $9+9+2$ insect sperm axoneme. Nine microtubule doublets (d) with associated dynein arms (da) and radial spokes (rs) are connected to two central microtubules (ct) via the central sheath (cs). The doublets are in turn surrounded by nine accessory tubules (at). Accessory tubules and doublets are linked together by intertubular material (itm). (*h*) Schematic cross-sectional drawing of an axonemal doublet showing the protofilament arrangement of the A and B subtubules. The radial spoke (rs), the inner dynein arm (ia) and the outer dynein arm (oa) are attached to the A subtubule. This figure and caption are reproduced with permission from Werner & Simmons [5]. Copyright 2008 John Wiley and Sons.

The structure of this paper is as follows. We idealize the double-wave structure as the propagation of superhelical waves and model the hydrodynamics using non-local slender body theory (SBT) in §2. In §3, we present the computed hydrodynamic performance of spermatozoa of different species and compare the predictions with the available experimental data (§3.1). The features of superhelical swimming are illustrated by a specific model organism, namely the spermatozoa of *Cu. melleus* (§3.2). We then investigate the effects of kinematic and geometric parameters on the propulsion performance of a superhelical swimmer (§3.3). Finally, the limitations of the present study and directions for future work are discussed in §4.

2. MATERIAL AND METHODS

2.1. Idealized double-wave structure: superhelical swimmers

The experimentally observed double-wave structure of insect spermatozoa is mathematically idealized in this paper as a superhelix (a small helix itself coiled into a larger helix); we refer to the helical structure with the larger wavelength as the major helix and the other as the minor helix. To mathematically describe a superhelix, we first construct the position vector of a regular axial helix (the major helix) to be $\mathbf{H}(s') = [A_\mathrm{M}\cos(k_\mathrm{M}\alpha s'), A_\mathrm{M}\sin(k_\mathrm{M}\alpha s'), \alpha s']$, with $\alpha = 1/\sqrt{1+A_\mathrm{M}^2 k_\mathrm{M}^2}$. Here k_M is the wavenumber, A_M is the amplitude, and $s' \in [0, L']$ and L' are the arc-length parameter and the length of the major helix, respectively. From this basic helix, the local unit tangent $\hat{\mathbf{t}}_A$, unit normal $\hat{\mathbf{n}}_A$ and unit binormal $\hat{\mathbf{b}}_A = \hat{\mathbf{t}}_A \times \hat{\mathbf{n}}_A$ vectors are determined, and we take them to define a local coordinate system upon which the minor helix is constructed [20]. The position vector of the combined superhelical shape is then given by:

$$\begin{aligned}\mathbf{X}(s') &= [x(s'), y(s'), z(s')] \\ &= \mathbf{H}(s') + A_\mathrm{m}\cos(k_\mathrm{m}s')\,\hat{\mathbf{n}}_A(s') \end{aligned} \tag{2.1}$$

$$\pm\, A_\mathrm{m}\sin(k_\mathrm{m}s')\,\hat{\mathbf{b}}_A(s'), \tag{2.2}$$

where A_m and k_m are the amplitude and wavenumber of the minor helix, respectively. Two different configurations will be considered: the '+' (plus) sign leads to a superhelical structure where both the major and minor helices have the same chirality, whereas the '−' (minus) sign represents the case of opposite chirality.

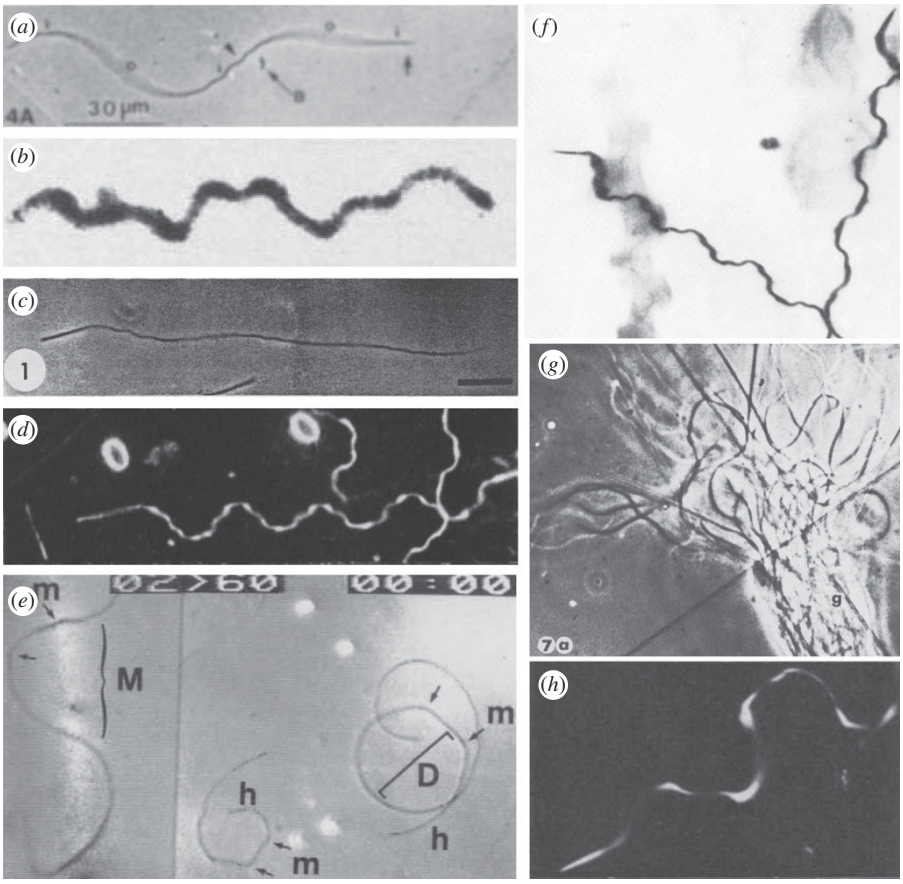

Figure 3. The double-wave beating pattern observed in insect spermatozoa flagella of different species: (*a*) *Megaselia scalaris* [18], (*b*) *Haematopinus suis* [6], (*c*) *Culicoides melleus* [14], (*d*) *Tenebrio molitor* [11], (*e*) *Drosophila obscura* [17], (*f*) *T. molitor* [13], (*g*) *Aedes notoscriptus* [15] and (*h*) *Bacillus rossius* [12]. All images were reproduced with permission: (*a*) from Curtis & Benner [18]. Copyright © 1991 John Wiley and Sons; (*b*) from Baccetti [6]. Copyright © 1972 Elsevier; (*c*) from Linley [14]. Copyright © 1979 John Wiley and Sons; (*d*) from Baccetti *et al.* [11]. Copyright © 1973 Plenum Publishing Corporation, with kind permission from Springer Science + Business Media B.V; (*e*) from Bressac *et al.* [17]. Copyright © 1991 John Wiley and Sons; (*f*) from Philips [13]. Copyright © 1974 John Wiley and Sons; (*g*) from Swan [15]. Copyright © 1981 John Wiley and Sons; (*h*) from Baccetti *et al.* [12]. Copyright © 1973 Elsevier.

Note that s' is no longer the natural arc-length parameter, but merely a regular parameter for describing the swimmer's geometry. The arc-length of the complete superhelix, denoted by s, as a function of the parameter s' is determined by numerical integration, and the total length of the superhelix is denoted by L.

The major and minor helices are free to propagate waves at different wave speeds. Denoting c_M and c_m as the major and minor wave speeds, respectively, the position vector at time t, $\mathbf{X}(s',t)$, may be written in component form as:

$$\begin{aligned} x(s',t) = {} & A_\mathrm{M}\cos[k_\mathrm{M}(\alpha s' - c_\mathrm{M}t)] \\ & - A_\mathrm{m}\cos[k_\mathrm{m}(s' - c_\mathrm{m}t)]\cos[k_\mathrm{M}(\alpha s' - c_\mathrm{M}t)] \\ & \pm \alpha A_\mathrm{m}\sin[k_\mathrm{m}(s' - c_\mathrm{m}t)]\sin[k_\mathrm{M}(\alpha s' - c_\mathrm{M}t)], \end{aligned} \tag{2.3}$$

$$\begin{aligned} y(s',t) = {} & A_\mathrm{M}\sin[k_\mathrm{M}(\alpha s' - c_\mathrm{M}t)] \\ & - A_\mathrm{m}\cos[k_\mathrm{m}(s' - c_\mathrm{m}t)]\sin[k_\mathrm{M}(\alpha s' - c_\mathrm{M}t)] \\ & \mp \alpha A_\mathrm{m}\sin[k_\mathrm{m}(s' - c_\mathrm{m}t)]\cos[k_\mathrm{M}(\alpha s' - c_\mathrm{M}t)], \end{aligned} \tag{2.4}$$

and

$$z(s',t) = \pm \alpha A_\mathrm{m} A_\mathrm{M} k_\mathrm{M}\sin[k_\mathrm{m}(s' - c_\mathrm{m}t)] + \alpha s'. \tag{2.5}$$

In addition to the long flagellum, insect spermatozoa have cell bodies that are very slender and short when compared with the flagellum size. We expect that the hydrodynamic influence of the sperm head is negligible and do not include such a body in our consideration. A typical superhelical swimmer is shown in figure 4 using the dimensionless parameters of *Cu. melleus* spermatozoa.

2.2. Hydrodynamic modelling

Flagellar swimming is a result of the interaction between the actuating body and the surrounding fluid. A tractable and accurate approach to studying such hydrodynamic interactions exploit the slenderness of the flagellum, in which the velocity along the flagellar centreline is related to the fluid forces along the same curve. In previous studies, the fluid–body interaction has been modelled using a resistive force theory (RFT) [21–23], in which local forces acting on the flagellum at any station along

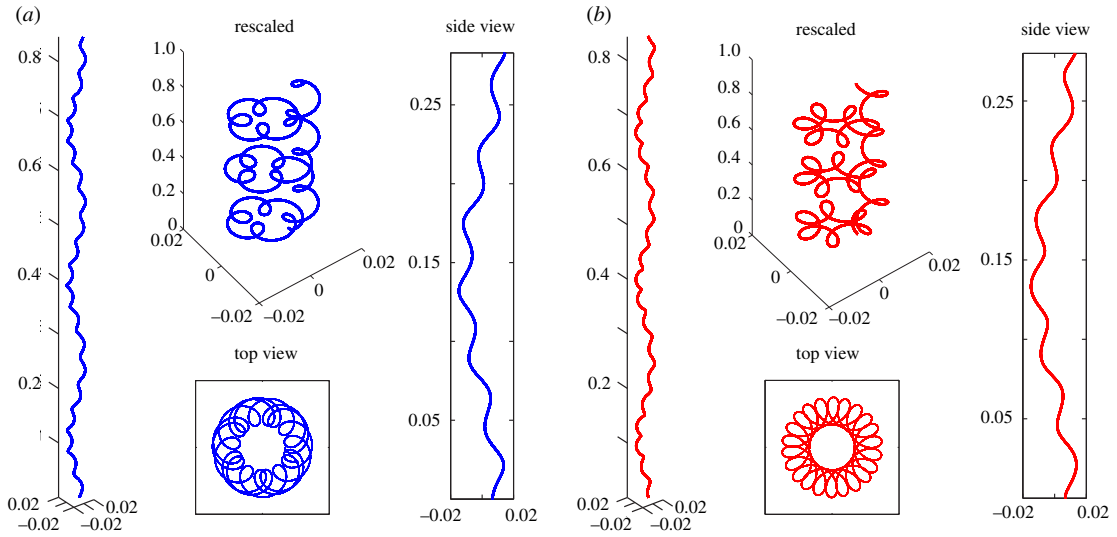

Figure 4. Idealization of the double-wave structure as superhelices for the (*a*) same-chirality, and (*b*) opposite-chirality configurations, using the dimensionless parameters of *Culicoides melleus* spermatozoa (table 2). (Online version in colour.)

the filament are expressed in terms of the local velocity at the same location. RFT takes only local effects into account and neglects any hydrodynamic interactions between different parts of the deforming body. The local theory works well for simple geometries. However, owing to the complexity of the superhelical structure in the problem under consideration here, the local theory is inadequate (see §3.4 for details), and we employ instead the full non-local SBT [24] to study the hydrodynamics of the superhelical swimmers. The non-local theory captures the hydrodynamic interactions between distant parts of a curved filament, while still taking advantage of the slenderness of flagellum to simplify the analysis.

The flagellum is modelled as a slender filament of length L and circular cross section of radius $\epsilon L r(s)$, where $\epsilon \ll 1$ is the small aspect ratio of the flagellum (the maximum radius along the flagellum a_r divided by its total length L) and $r(s)$ is the dimensionless radius. The non-local SBT is algebraically accurate in ratio of the slenderness ϵ; namely, by setting the radius profile to $r(s) = \sqrt{4s(L-s)}/L$, the computed fluid velocity is accurate to $O(\epsilon^2)$ [24].

For a given velocity distribution $\mathbf{v}(s,t)$ along the filament at time t, the corresponding fluid force per unit length $\mathbf{f}(s,t)$ is given implicitly by the non-local relation

$$8\pi\mu\mathbf{v}(s,t) = -\Lambda[\mathbf{f}(s,t)] - \mathbf{K}[\mathbf{f}(s,t)], \tag{2.6}$$

where

$$\Lambda[\mathbf{f}](s,t) = [c_0(\mathbf{I}+\hat{\mathbf{t}}\hat{\mathbf{t}}) + 2(\mathbf{I}-\hat{\mathbf{t}}\hat{\mathbf{t}})]\mathbf{f}(s,t), \tag{2.7}$$

and

$$\mathbf{K}[\mathbf{f}](s,t) = (\mathbf{I}+\hat{\mathbf{t}}\hat{\mathbf{t}})\int_0^L \frac{\mathbf{f}(\tilde{s},t)-\mathbf{f}(s,t)}{|\tilde{s}-s|}\mathrm{d}\tilde{s} + \int_0^L \left(\frac{\mathbf{I}+\hat{\mathbf{R}}\hat{\mathbf{R}}}{|\mathbf{R}(\tilde{s},s;t)|} - \frac{\mathbf{I}+\hat{\mathbf{t}}\hat{\mathbf{t}}}{|\tilde{s}-s|}\right)\mathbf{f}(\tilde{s},t)\mathrm{d}\tilde{s}, \tag{2.8}$$

are the local and non-local operators, respectively, μ is the shear viscosity of the fluid, $c_0 = -\ln(\epsilon^2 \mathrm{e}) > 0$, $\mathbf{R}(\tilde{s},s;t) = \mathbf{X}(\tilde{s},t) - \mathbf{X}(s,t)$, $\hat{\mathbf{R}} = \mathbf{R}/|\mathbf{R}|$ and $\hat{\mathbf{t}}$ is the local unit tangent vector at the point s.

The swimmers of interest deform their shapes in a prescribed, time-varying fashion (the superhelical wave pattern, equations (2.3)–(2.5)), and the velocity created on its surface by this deformation is given by $\mathbf{v}_{\mathrm{deform}}(s,t) = \partial\mathbf{X}(s,t)/\partial t$. At every time instant t, the swimmer can be seen as a solid body with unknown translational velocity $\mathbf{U}(t)$ and rotation rate $\boldsymbol{\Omega}(t)$. The velocity created on the swimmer's surface owing to swimming is then $\mathbf{v}_{\mathrm{swim}}(s,t) = \mathbf{U} + \boldsymbol{\Omega}\times[\mathbf{X}(s,t) - \mathbf{X}_0]$, where $\mathbf{X}_0$ is an arbitrary reference point (taken as the origin here for simplicity). Therefore, the local velocity relative to the fluid $\mathbf{v}(s,t)$ is given by the sum of the deformation and swimming velocities: $\mathbf{v}(s,t) = \mathbf{v}_{\mathrm{deform}} + \mathbf{v}_{\mathrm{swim}} = \mathbf{U} + \boldsymbol{\Omega}\times[\mathbf{X}(s,t) - \mathbf{X}_0] + \partial\mathbf{X}(s,t)/\partial t$. In this work, the wave propagation is towards the positive z-direction. Therefore, a negative swimming velocity ($\mathbf{U}$) means that the propulsion occurs in a direction opposite to the wave propagation, while a positive swimming velocity means that both the propulsion and wave propagation occur in the same direction.

Using a Galerkin method [25], we express the local force $\mathbf{f}(s,t)$ as a finite sum of Legendre polynomials and solve equation (2.6) for $\mathbf{f}(s)$ by requiring the equation to hold under inner products against the same basis functions. The first integral in the non-local operator $\mathbf{K}[\mathbf{f}]$ is diagonalized in this space [26,27]. The system is closed by requiring the entire swimmer to be force-free and torque-free,

$$\int_0^L \mathbf{f}(s)\mathrm{d}s = 0, \tag{2.9}$$

and

$$\int_0^L [\mathbf{X}(s) - \mathbf{X}_0]\times\mathbf{f}(s)\mathrm{d}s = 0, \tag{2.10}$$

providing at each moment in time a system of six equations to solve for the six unknowns $\mathbf{U}(t)$ and $\mathbf{\Omega}(t)$.

The swimming velocities determined in the manner described above represent velocities in a reference frame fixed on the swimmer. In order to study the full three-dimensional swimming kinematics in the laboratory frame (in which the body moves with velocity $\tilde{\mathbf{U}}(t)$ and rotation rate $\tilde{\mathbf{\Omega}}(t)$), we must include a transformation between the two. We denote the Cartesian coordinate system moving with the swimmer, the body frame, as $[\mathbf{e}_x, \mathbf{e}_y, \mathbf{e}_z]$ and the Cartesian coordinate system in the laboratory frame as $[\mathbf{e}_1, \mathbf{e}_2, \mathbf{e}_3]$. The evolution of the body frame, with respect to the laboratory frame, is then governed by:

$$\frac{\mathrm{d}\mathbf{E}}{\mathrm{d}t} = \mathbf{\Omega}(t) \times \mathbf{E}, \tag{2.11}$$

where $\mathbf{E} = [\mathbf{e}_x, \mathbf{e}_y, \mathbf{e}_z]^{\mathrm{T}}$, along with the initial condition $[\mathbf{e}_x, \mathbf{e}_y, \mathbf{e}_z](t = 0) = [\mathbf{e}_1, \mathbf{e}_2, \mathbf{e}_3]$.

2.3. Non-dimensionalization

The process of non-dimensionalization is very useful in science and engineering to identify the relevant dimensionless parameters governing the physics of the problem. In theoretical studies, it always allows a more concise description of the system, while in experimental studies, it reduces the number of independent experiments required to fully explore the problem. The present system is made dimensionless by scaling lengths of the order of $1/k_{\mathrm{m}}$, velocities by c_{m} and time by their ratio, $1/c_{\mathrm{m}}k_{\mathrm{m}}$. The dimensionless position vector describing the kinematics of the superhelix is thus given by:

$$x = R\{\cos[K(\alpha s' - ct)] - r\ \cos(s' - t)\cos[K(\alpha s' - ct)] + \alpha r\ \sin(s' - t)\sin[K(\alpha s' - ct)]\}, \tag{2.12}$$

$$y = R\{\sin[K(\alpha s' - ct)] - r\cos(s' - t)\sin[K(\alpha s' - ct)] - \alpha r\sin(s' - t)\cos[K(\alpha s' - ct)]\}, \tag{2.13}$$

and

$$z = \alpha s' + \alpha r R^2 K \sin(s' - t), \tag{2.14}$$

where all variables are now understood to be dimensionless. Four dimensionless parameters characterizing the kinematics are identified above: the dimensionless amplitude of the major helix, $R = A_{\mathrm{M}}k_{\mathrm{m}}$, the ratio of the wavenumbers characterizing the major and minor helices, $K = k_{\mathrm{M}}/k_{\mathrm{m}}$, the ratio of the minor helix amplitude to the major helix amplitude, $r = A_{\mathrm{m}}/A_{\mathrm{M}}$ and the ratio of the major wave speed to the minor wave speed $c = c_{\mathrm{M}}/c_{\mathrm{m}}$. In the double-wave pattern observed in insect spermatozoa, the major wave amplitude is always larger than the minor wave amplitude ($r < 1$; although this need not be true for a general superhelix). In addition, it is also observed that the minor wave speed is always greater than the major wave speed in the double-wave structure of insect spermatozoa ($c < 1$).

2.4. Kinematic and geometric data

From the non-dimensionalization above, we have identified four dimensionless parameters (r, R, K, c) required to fully characterize the centreline motion of a superhelical flagellum. Werner & Simmons [5] have compiled a very useful table containing kinematic and geometric data of the double-wave structure observed in insect spermatozoa in previous studies. The table reveals that experimental measurements of the necessary quantities for hydrodynamic modelling are very limited owing to the difficulties involved in interpreting three-dimensional data from two-dimensional images [14].

Here, we follow the table compiled by Werner and Simmons and estimate the missing information based on images of insect spermatozoa reported in the literature. Table 1 contains reported and estimated data on the double-wave structure, including the wavelengths, amplitudes, frequencies, major and minor wave speeds, flagellum thickness, and the swimming speed of different insect spermatozoa. Our estimated quantities are marked with asterisks to distinguish them from reported quantities by the original papers. In some studies (e.g. for *Lygaeus* [13]), only relative lengths can be given because of the lack of scale bars in the reported images; these relative quantities are square-bracketed in tables 1 and 2. Geometric and kinematic data can display large variations even within a species (*T. molitor* [11]). When the distribution of the quantities are not given, arithmetic means of the available measurements are used whenever appropriate in the present study.

The measurements are presented in the corresponding dimensionless quantities in table 2, using the scalings defined in §2.3. We have not found any information in the referenced literature about the chirality of the major and minor helical structures. We therefore present results below for both the same-chirality and opposite-chirality configurations. In our measurements (collected in table 1), the wavelength of the minor wave is taken to be the two-dimensional distance between adjacent minor wave peaks. A small correction factor is required to convert these two-dimensional quantities to the appropriate wavelengths in describing the three-dimensional superhelical structure. The correction factor depends on whether the superhelical structure is in the same-chirality ($1/(1 - \alpha\lambda_{\mathrm{m}}/\lambda_{\mathrm{M}})$) or in the opposite-chirality ($1/(1 + \alpha\lambda_{\mathrm{m}}/\lambda_{\mathrm{M}})$) configuration.

3. RESULTS

In this section, we first use the framework described above to predict the swimming performance of spermatozoa of different species, and compare our hydrodynamic results with the available experimental measurements. We then illustrate the basic features of superhelical swimming by focusing on a model organism, namely *Cu. melleus*, and proceed to perform a parametric study investigating the effects of certain kinematic parameters (minor and major wave speeds) and geometric parameters (minor and major wave amplitudes).

Table 1. Kinematic and geometric data of the double-wave structure. (We follow the table by Werner & Simmons [5] with our estimations (marked with asterisks) of the missing quantities based on the images of the sperm cell reported in the references; a_r refers to the radius of the flagellum.)

	major wave				minor wave						
species	λ_M(μm)	A_M(m)	f_M (Hz)	c_M (μm/S)	λ_β (μm)	A_m (μm)	f_m (Hz)	c_m (μm/s)	$2a_r$ (μm)	V_{sperm} (μm)	references
Aedes notoscriptus	28*	3.67*	3.4	95.2*	6.8*	1.83*	34	231.2*	0.55*		Swan *et al.*[15]
Bacillus Rossius	40*	12	12	480*	17.9*	1.1	40	716*	0.74*		Baccetti *et al.* [12]
Ceratitis capitata[a]	30	20	4	120*	7–8	1–2	20	150*	0.68*	16	Baccetti *et al.* [16]
Culicoides melleus	54.1	2.1			8.7	0.8	8.2	80	0.77*	8.3	Linley [14]
Drosophila obscura[b]	45*	16			13.3*	0.5*	20.4	271	0.76*		Bressac *et al.* [17]
Lygaeus[c]	[1]*	[0.1]*			[0.21]*	[0.014]*	130		[0.024]*		Phillips [13]
Megaselia scalaris	68*	9.3*	3.1	210.8*	7*	0.5*			0.78*	12.7	Curtis & Benner [18]
Tenebrio molitor[d]	20–30 (25)	9–15 (12)	0.9–2.8 (1.85)	20–90 (55)	6–12 (9)	3–4 (3.5)	7–28 (17.5)	40–300 (170)	0.79*	16–100 (58)	Baccetti *et al.* [11]

[a]Only forward mode is considered [16].
[b]Only male long sperm is considered here [17].
[c]Scale bars were not presented with the images in the reference and only relative lengths (square-bracketed) can be estimated.
[d]Round brackets denote arithmetic means.

Table 2. Dimensionless parameters of superhelical flagella: $K = k_M/k_m$; $R = A_M k_m$; $r = A_m/A_M$; $c = c_M/c_m$; $V = V_{sperm}/c_m$; $a = a_r k_m$; n refers to number of large wavelengths. ($\tilde{U}_+$ *and* $\tilde{U}_-$ are the predicted average swimming velocities for the same-chirality and opposite-chirality s configurations, respectively.)

species	K	R	r	c	N	a	V	$\tilde{U}_+$ ($\tilde{U}_-$)	η_+ (η_-)(%)	$\lvert \tilde{U}_+ - V\rvert/V$ ($\lvert \tilde{U}_- - V\rvert/V$) (%)
Aedes notoscriptus	0.24*	3.4*	0.5*	0.41*	1	0.25*		0.21 (0.16)	1.2 (0.34)	
Bacillus rossius	0.45*	4.2*	0.092	0.67*	1.5	0.13*		0.031 (0.033)	0.30 (0.14)	
Ceratitis capitata	0.25	16.8	0.075	0.8*	4–5[a]	0.28*	0.11*	0.15 (0.039)[c]	0.40 (0.021)	36 (65)
Culicoides melleus	0.16	1.5	0.38		3	0.28*	0.10	0.051 (0.15)	0.30 (1.5)	49 (50)
Drosophila obscura	0.30*	7.6*	0.03*		1	0.18*		0.012 (0.0096)	0.10 (0.036)	
Lygaeus	0.21*	3*	0.14*		1–2[b]	0.34*		0.033 (0.081)	0.24 (0.71)	
Megaselia scalaris	0.10*	8.3*	0.05*		1	0.35*		0.035 (0.065)	0.16 (0.42)	
Tenebrio molitor	0.36	8.4	0.29	0.32	4	0.28*	0.34	0.40 (0.41)[d]	1.2 (0.86)	18 (21)

[a]A value of 4 is adopted in the simulation.
[b]A value of 1 is adopted in the simulation.
[c]Velocity in the z-direction occurs in the same direction as the wave propagation.
[d]Velocity in the z-direction occurs in the same direction as the wave propagation.

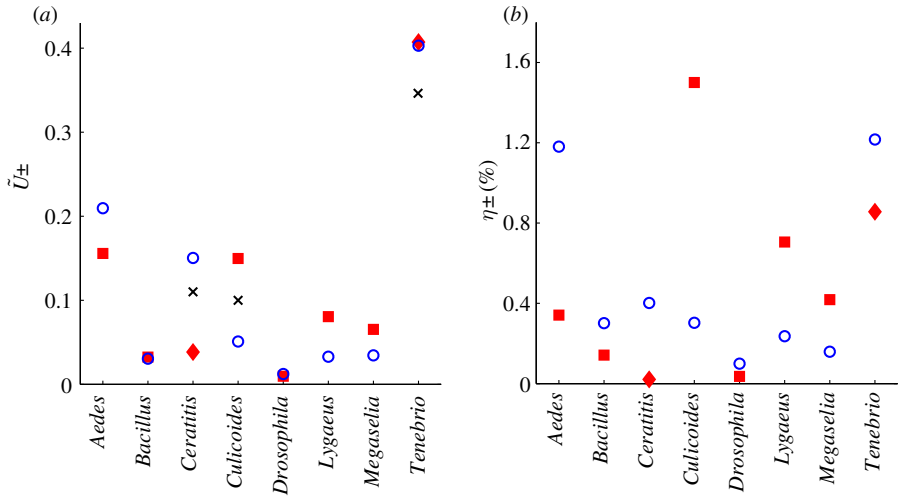

Figure 5. Predicted swimming performance: (*a*) average swimming speed, $\tilde{U}_{\pm}$, of different species; (*b*) hydrodynamic efficiency, $\eta_{\pm}$, of different species. Open symbols (blue circles) represent the same-chirality configuration (+); filled symbols (red squares and diamonds) represent the opposite-chirality configuration (−); for blue open circles and red squares, swimming occurs in the opposite direction as the wave propagation; on the contrary, red diamonds represent the cases of opposite-chirality configuration where the velocity in the *z*-direction occurs in the same direction as the wave propagation; black crosses represent experimental measurements of $V = V_{\mathrm{sperm}}/c_{\mathrm{m}}$ (see tables 1 and 2). (Online version in colour.)

3.1. Hydrodynamic performance

3.1.1. Propulsion speed

The propulsion speed is an important functional parameter characterizing the motility of a sperm cell. There exist only very few measurements of the swimming speed of insect spermatozoa exhibiting the double-wave structure: *Ce. capitata* was observed to swim at a speed, $V_{\mathrm{sperm}} = 16\ \mu\mathrm{m\,s^{-1}}$ [16] and the minor wave speed is estimated to be $150\ \mu\mathrm{m\,s^{-1}}$ (hence, $V = V_{\mathrm{sperm}}/c_{\mathrm{m}} = 0.11$); *Cu. melleus* [14] was observed to swim at a speed of $8.3\ \mu\mathrm{m\,s^{-1}}$ and minor wave speed of $80\ \mu\mathrm{m\,s^{-1}}$ ($V = 0.10$). For the case of *T. molitor*, a wide range of sperm speeds were reported (from 16 to $100\ \mu\mathrm{m\,s^{-1}}$) as well as minor wave speeds (40–$300\ \mu\mathrm{m\,s^{-1}}$) [11]. The distributions were not reported however; so using the arithmetic means we obtain a swimming speed to minor wave speed ratio of $V = 0.34$.

For a superhelical swimmer in our model, the swimming kinematics are three-dimensional and unsteady in time,[1] and the most relevant quantification of the propulsion speed is an average swimming velocity in the laboratory frame, denoted by $\tilde{U}_{\pm}$, where the + (plus) and − (minus) signs represent the same- and opposite-chirality configurations, respectively. The average swimming speed is defined as $\tilde{U}_{\pm} = |[\langle \tilde{U}_x \rangle, \langle \tilde{U}_y \rangle, \langle \tilde{U}_z \rangle]|$, where $|\cdots|$ denotes the magnitude of a vector, and $\langle \cdots \rangle$ denotes a time average.[2] Since the chirality configuration remains unknown, we present predictions for both cases in figure 5*a*. Only the three sets of experimental measurements of the swimming performance ($V = V_{\mathrm{sperm}}/c_{\mathrm{m}}$) mentioned above are available for comparison and are superimposed on the same figure (figure 5). Predictions as ratios of the swimming speed relative to the minor wave speed (dimensionless speed) for species with no measurement of V are also provided in figure 5*a*.

In most of the cases considered, the propulsion in the longitudinal direction (*z*-direction) of these superhelical swimmers is opposite to the direction of wave propagation (the major wave propagates in the positive *z*-direction, and the minor wave propagates along the curved major helix and distally towards the positive *z*-direction), regardless of the chirality configuration. This is not unlike the behaviour of swimmers propagating a planar sinusoidal or a regular helical wave, for which the swimming direction is also opposite to the direction of the wave propagation. In superhelical swimming, however, we also find cases of the opposite-chirality configuration, where the body swims in the same direction as the wave propagation. Specifically, we note a qualitative difference between the study of the same-chirality and opposite-chirality configurations for *Ce. capitata* and *T. molitor*. In these simulations, a superhelical wave is set to propagate in the positive *z*-direction, and both the opposite-chirality configurations of *Ce. capitata* and *T. molitor* generate a positive U_z (swimming is in the same direction as the wave propagation), while their corresponding same-chirality configurations generate a negative U_z (swimming is in the opposite direction as the wave propagation). The speed and efficiency of these peculiar swimmers are distinguished from other cases by red diamonds as shown in figure 5. It remains a question whether this phenomenon may be observed in nature, as the chirality configuration and the swimming direction (relative to the wave propagation) of actual insect spermatozoa displaying the double-wave

[1]The deformations (equations (2.3)–(2.5)) are higher frequency oscillations modulated by lower frequency oscillation (a beat). There does not exist a time period T, such that the deformation vector repeats itself: $\mathbf{R}(s,t+T) \neq \mathbf{R}(s,t)$, $\forall T$.

[2]The time averaging is defined for a function $f(t)$ as $\int_0^{t_0} f(t)\ \mathrm{d}t/t_0$, where t_0 is a sufficiently large time, such that the peak-to-peak fluctuation in time is less than 1 per cent of the final average value.

structure are still unclear. Nevertheless, this phenomenon by itself is intriguing and will be further explored in §3.3.1.

The swimming speed predictions lie at least within the same order of magnitude of the experimental measurements for both chirality configurations. The same-chiralty results provide slightly better agreement than the opposite-chiralty results (without taking the swimming direction into account). For the same-chirality configuration, the discrepancies, $|\tilde{U}_+ - V|/V$, between the predictions and the experimental measurements read 36 per cent for *Ce. capitata*, 49 per cent for *Cu. melleus* and 18 per cent for *T. molitor*. For the opposite-chirality configuration, the discrepancy between our predictions and the experimental measurements, $|\tilde{U}_- - V|/V$, are 65 per cent for *Ce. capitata*, 50 per cent for *Cu. melleus* and 21 per cent for *T. molitor*. Given the primitive nature of the data employed (see §2.4), we consider the agreements here to be reasonable. However, we cannot draw definite conclusions on the issue of chirality configuration; further experimental observations are necessary.

It shall be remarked that the present study is largely constrained by the unavailability of experimental measurement data. Critical kinematic information, such as the major and minor wave speeds, are often not reported in the literature and are impossible to estimate from the images available. The speed ratio $c = c_M/c_m$ is not available for simulations for most species. The computations here are still possible because of the independence of the swimming kinematics on the parameter c (verified numerically and will be explained in §3.3.1). Therefore, the specific value of c is unimportant for all cases considered here; we adopt $c = 0$ in all simulations hereafter unless otherwise stated.

3.1.2 Hydrodynamic efficiency

Another important functional parameter is the hydrodynamic efficiency of the swimmer. In the microscopic world, the hydrodynamic efficiency is typically very low. For a rigid helix, Lighthill [28] calculated theoretically the maximum efficiency attainable to be about 8.5 per cent, while the typical efficiency of biological cells is around 1–2% [3,28–32]. For low Reynolds number swimming, a common measure of the hydrodynamic efficiency, η, is the ratio of the rate of work required to drag the straightened flagellum through the fluid to the rate of work done on the fluid by the flagellum during swimming [28],

$$\eta_\pm = \frac{\xi_\parallel L\, \tilde{U}_\pm^2}{\langle \int_0^L \mathbf{v}\cdot\mathbf{f}\,\mathrm{d}s\rangle}, \tag{3.1}$$

where $\xi_\parallel = 4\pi/c_0$ is the drag coefficient for a straight, slender rod, and the brackets indicate a time average. We calculate the hydrodynamic efficiencies for both the same- and opposite-chirality configurations (figure 5*b*) for spermatozoa of different species. For the same-chirality configuration, the efficiency ranges from 0.16 per cent (*M. scalaris*) to 1.2 per cent (*Ae. notoscriptus* and *T. molitor*); for the opposite-chirality configuration, the efficiency ranges from 0.036 per cent (*Dro. obscura*) to 1.5 per cent (*Cu. melleus*). The efficiencies of these swimmers are comparable with typical biological cells.

3.2. Model organism: Cu. melleus

In this section, we illustrate the features of superhelical swimming by singling out a superhelical swimmer defined using the geometric data of the sperm cell of *Cu. melleus* (table 2). See figure 4 for the swimmer geometry.

3.2.1. Swimming kinematics

The swimming velocities computed for motion in the body frame $[U_x, U_y, U_z]$ and in the laboratory frame $[\tilde{U}_x, \tilde{U}_y, \tilde{U}_z]$ of the superhelical swimmer with data from the sperm cell of *Cu. melleus* are plotted in figure 6 for the same-chirality (figure 6*a*) and opposite-chirality (figure 6*b*) configurations. We include in these figures the results for the ratio of the major and minor wave speeds $c = 0$ (solid lines) and $c = 0.4$ (dotted lines). When $c = 0$, the deformation (equations (2.12)–(2.14) is 2π-periodic, therefore the swimming kinematics in the body frame are also 2π-periodic. However, when observed in the laboratory frame, the coupling between the translational and rotational kinematics renders the swimming velocities no longer 2π-periodic, and the motion is unsteady in time (figure 6*c*,*d*). We observe a pattern consisting of higher frequency oscillations modulated by a lower frequency envelope. For the case of $c = 0.4$, when observed in the body frame, we see modulated waveforms. However, when transformed to the laboratory frame, the cases of $c = 0$ and $c = 0.4$ have identical swimming kinematics (see the overlapped solid and dotted lines in figure 6*c*,*d*), implying that the swimming kinematics in the laboratory frame are independent of the major propagating wave speed. The value of c affects only the kinematics in the body frame; why the relative wave speed is unimportant is described in greater detail in §3.3.1.

The three-dimensional swimming velocities give rise to a doubly-helicated trajectory (the presence of a minor structure on top of a major helical structure). However, this could be difficult to observe experimentally as the major amplitude of the doubly-helicated trajectory is usually much smaller than that of the superhelical swimmer; the swimmer would apparently move with a straight trajectory (with very small oscillations in the transverse direction). Recall that for regular helical swimming ($r = 0$), the trajectory of the helical swimmer reduces to a regular helix.

3.2.2. Head-less swimming

The shape and size of the sperm head vary among spermatozoa of different species: human and bull spermatozoa have relatively large, paddle-shaped heads, whereas insect spermatozoa have elongated heads which are almost indistinguishable from the mid-piece. The additional hydrodynamic resistance from the presence of a head would seemingly degrade the swimming performance of the sperm cell. However, Chwang & Wu [33] showed that a sperm head is actually necessary for helical swimming; without one, the motion is that of a rotating rigid body, which cannot be realized in the absence of an external force or torque [34]. To satisfy the zero

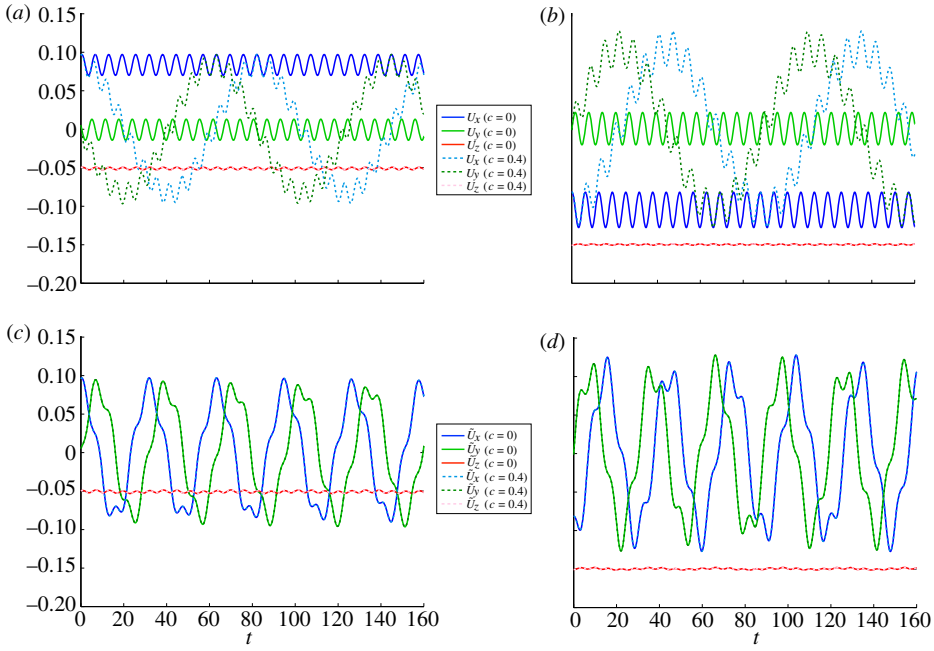

Figure 6. Three-dimensional swimming velocities in the body frame $\mathbf{U} = (U_x, U_y, U_z)$ for (*a*) the same-chirality and (*b*) the opposite-chirality configurations, and in the laboratory frame $\tilde{\mathbf{U}} = (\tilde{U}_x, \tilde{U}_y, \tilde{U}_z)$ for (*c*) the same-chirality and (*d*) the opposite-chirality configurations, for *Cu. melleus* spermatozoa. (Online version in colour.)

net-torque condition, a sperm head is required to balance the reaction torque acting on the flagellum. This constraint does not apply for planar, sinusoidal wave motion, which can swim without an anchor or load.

We pause to point out a subtle but important difference between a rotating prokaryotic helical tail and a eukaryotic tail propagating a bending helical wave. For a eukaryotic tail propagating a bending wave, the fluid forces act to rotate the flagellum opposite to the direction of the apparent helical rotation. The rotation owing to the fluid reaction creates torques owing to local spinning (rotation of the flagellum about its centreline), which balance the opposing torque generated by the helical wave propagation. Therefore, a eukaryotic cell could theoretically swim without a sperm head, albeit very slowly because the flagellum is very slender and the local torques are correspondingly small. Quantitatively, using a local drag model [33], it can be shown that the head-less swimming speed scales as $U/c \sim 2\mu k^2/\xi_{\|}(1 + k^2A^2)b^2 + O(b^4)$, where b is the radius of a cross section of the flagellum, and k and A are the wavenumber and helical radius, respectively. Using the geometrical data of flagella of *Euglena viridis* summarized by Brennen & Winet [4], and assuming a flagellar diameter of $2b \approx 0.25\ \mu$m [35,36], we find $U/c \approx 10^{-3}$. For a prokaryotic tail, however, the helix rotates as a rigid body. In this case, the local spinning torques generated by the active helical rotation and the passive rotation owing to the fluid reaction are identical in magnitude but opposite in sign. The torque-free condition therefore requires that the fluid reaction counter-rotates the helix at precisely the rotation rate of the helical wave propagation. Hence, there can be no effective helical rotation, and the body cannot swim. Although head-less swimming is theoretically possible for eukaryotic tails, the swimming speed would be exceptionally small as shown by the estimation above. The subtle difference between the two types of helical waves just described is often therefore neglected, and it is generally reasonable to state that head-less swimming is not possible using helical wave propagation.

In superhelical swimming, a sperm head is not required for self-propulsion (indeed, all cases reported in this paper were studied with the absence of a sperm head) as a superhelical wave motion is in general not a rigid body motion. Furthermore, as actual insect spermatozoa heads are very slender and short when compared with the entire length of the flagellum, the contribution of its hydrodynamic resistance and the hydrodynamic interactions with the flagellum should be negligible. Therefore, we do not expect the presence of a slender and short sperm head to introduce qualitative differences in the results.

3.3. Parametric study

Next, we explore the effects of certain kinematic (wave speeds) and geometric parameters (wave amplitudes) on the swimming velocities of a superhelical swimmer.

3.3.1. The effect of the major/minor wave speed ratio

In this problem we have scaled the velocities upon the minor wave speed c_{m}, which implies that the dimensionless swimming velocities scale linearly with the minor wave speed. Here, we examine the effect of the major wave speed on the swimming performance of a superhelical swimmer and answer the question: to what relative extent do the two waves contribute to the propulsion of the superhelical swimmer [14]? Specifically, we study the effect of the parameter

$c = c_M/c_m$, which is the ratio of the major wave speed to the minor wave speed. For every species shown in table 2, we fix all parameters but vary the value of c from zero to unity ($c < 1$, as $c_M < c_m$). It is found that the swimming velocities in the laboratory frame is independent of the value of c. We have already shown in figure 6 the results for two values of c for illustration. While the resulting swimming motions in these two cases differ significantly in the body frame, they are identical when observed in a laboratory frame of reference. The numerical results imply that the major wave speed does not contribute to propulsion.

These findings may be understood by noting an ambiguity in definition. First consider a single helical filament (without a sperm head) placed in a fluid. Such a body cannot swim on its own, for there is no load or cell to counterbalance the torque it would exert on the surrounding fluid during rotation, so it must be motionless as seen in a fixed, laboratory frame. However, this body may be represented as an active helical body propagating a wave with velocity c plus a rigid body rotation that contributes a wave with speed $-c$. That the body frame may be chosen arbitrarily allows for such an ambiguity in the definition of the swimming speed, but in the laboratory frame this ambiguity disappears.

A similar argument can be used to show that c has no bearing on the swimming speed of a superhelical flagellum in the laboratory frame. For a superhelical flagellum, the propagation of the major wave can be defined as a rigid body rotation of the entire superhelical structure about the longitudinal axis (z-axis) in the body frame. The apparent rotation rate is the sum of the rotation caused by the active propagation of the major wave and the rotation caused by fluid reaction to maintain the force-free and torque-free conditions. For swimming without a head, only the apparent rotation rate is important because the fluid forces and torques are functions of the apparent rotation rate alone (not the absolute value of the rotation rate owing to the active major wave propagation). Any alternation of the major wave speed is accompanied by a corresponding change in the rotation rate caused by the fluid reaction, resulting in the same apparent rotation rate and the same force and torque balances. Therefore, the kinematics and dynamics do not depend on the absolute value of the major wave speed c (or c_m). In other words, the major wave speed does not contribute to swimming.

For the case of swimming with a head, the fluid reaction will not only rotate the flagellum but also the sperm head, which creates extra torques and perturbs the original force and torque balances. Altering the absolute value of the major wave speed in this case theoretically will affect the swimming velocities even in the laboratory frame, because it changes the relative portion of the rotation rate caused by the fluid reaction and hence the value of the extra torque from the sperm head. However, as the sperm head is slender and short when compared with the overall length of the flagellum of actual insect spermatozoa, the extra-resistant forces and torques created should be insignificant. Therefore, we suggest that the propagation of the major wave contributes very little to the propulsion (none in the case of head-less swimming), and that it is the minor wave speed that is primarily responsible for the propulsion. Note also that the hydrodynamic efficiencies in §3.1.2 are independent of the value of c. Therefore, from a hydrodynamic efficiency point of view, there is no advantage or disadvantage to actively propagate a major wave. However, there are other energy costs not taken into account here (for example, work done to produce the sliding of microtubules within the flagellum) in actively propagating a major wave. Therefore, we speculate that it might be energetically more favourable for a doubly helicated organism to propagate only a minor wave.

3.3.2. The effects of the parameters R *and* r

We now examine the effect of geometrical dimensionless parameters R and r, keeping all other parameters of *Cu. melleus* spermatozoa fixed. R is the dimensionless major wave amplitude and r is the ratio of minor to major wave amplitude, hence the minor wave amplitude is given by rR (see the schematic in figure 7). In general, one expects the propulsion speed to increase with the wave amplitude for simple geometries. However, for a superhelical structure, the dependence of the average swimming speed on the minor wave amplitude displays interesting behaviour. Physically, both the propulsive force and the bulkiness of the structure are varied upon changing the major or minor wave amplitudes. The competition between these factors and the coupling between kinematics in different directions create interesting geometric dependencies of the average swimming speed. We illustrate this by observing the average swimming speed under different frames of reference.

First, we look at the time-averaged swimming velocity in the body frame $U_b = |[\langle U_x(t)\rangle, \langle U_y(t)\rangle, \langle U_z(t)\rangle]|$. As shown in figure 7*a*(i), for the same-chirality configuration, the average swimming velocity grows monotonically with R and r. Note that, keeping other parameters fixed, increasing the value of $R = A_M k_m$ for a fixed $r = A_m/A_M$ geometrically means that both the major A_M and minor A_m amplitudes are increased simultaneously by the same proportion. There is a competition between the increase in the overall hydrodynamic resistance owing to the increased bulkiness (correlated with increases in A_M and A_m) and an enhanced propulsive force (correlated with an increase in A_m). In the case of the same-chirality configuration, the latter effect dominates. However, for the opposite-chirality configuration, as shown in figure 7*a*(ii), non-monotonic variations in the swimming speed with the major amplitude R are observed for certain values of r, the ratio of the minor to major wave amplitudes.

Since the swimming kinematics are three-dimensional, variations of the geometric parameters affect swimming velocities and rotational rates in all directions. In particular, a large propulsion speed in the body frame does not necessarily imply a large net propulsion speed in the laboratory frame. The mean swimming speeds in the laboratory frame for both chirality configurations are shown in figure 7*b*(i–ii). The coupling between the swimming kinematics in all directions

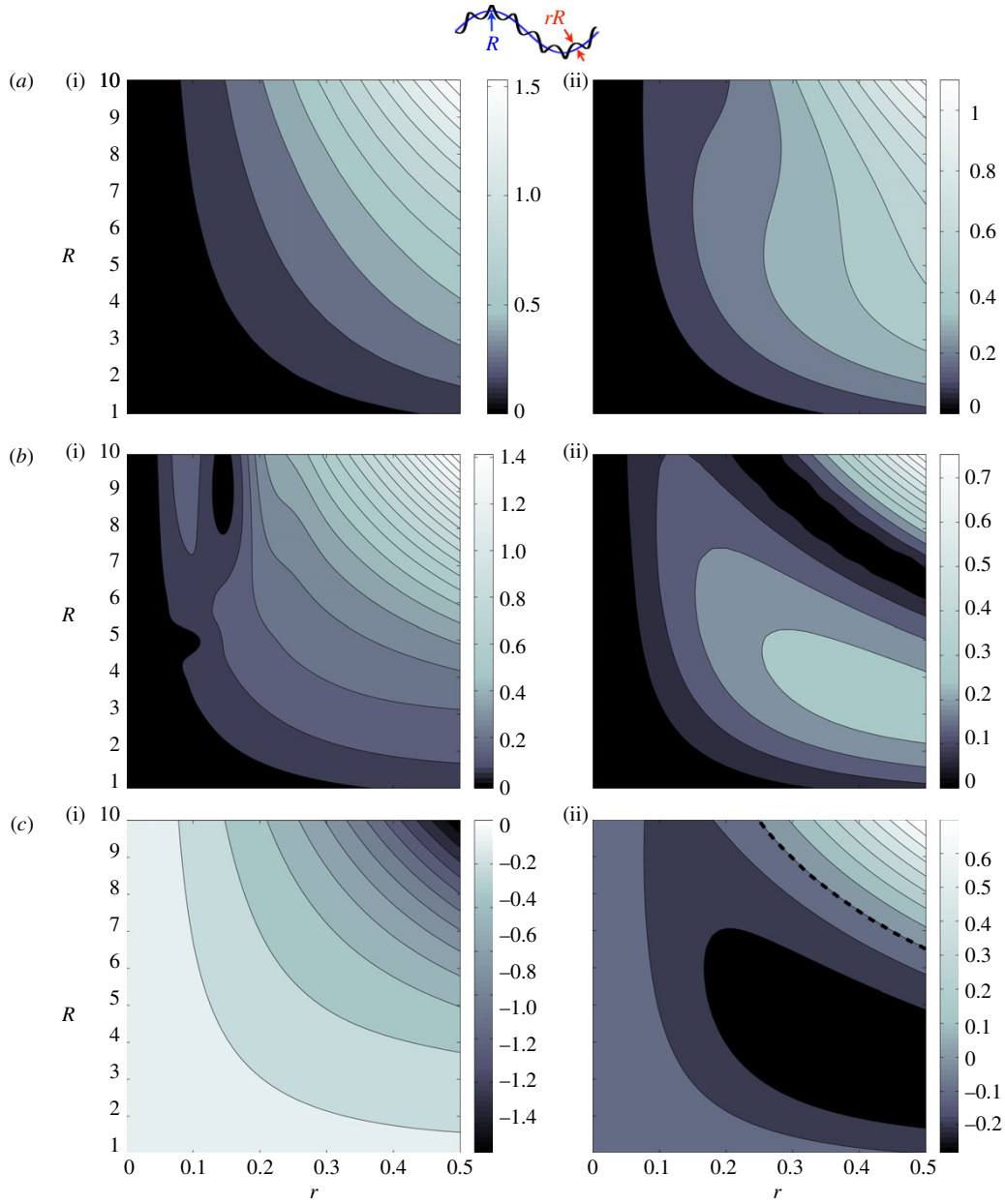

Figure 7. Parametric study of the dependence of the average swimming speed in the body-fixed frame U_b (a(i),(ii)) and in the laboratory frame $\tilde{U}_{\pm}$ (b(i),(ii)) as a function of the dimensionless parameters R and r (see the schematic for geometrical illustration). (c(i),(ii)) show the average swimming velocity in the z-direction in the body frame, $\langle U_z \rangle$, as a function of R and r. (a–c) on the left (right) refer to the same- (opposite-) chirality configuration. The dotted line in panel (c(ii)) represent the contour of $\langle U_z \rangle = 0$. Geometric data of *Cu. melleus* spermatozoa are used for other fixed parameters. (Online version in colour.)

produces more complicated variations in the propulsion speed as a function of R and r. Non-monotonic behaviours are observed in both cases.

We have already noted that some superhelical swimmers propel themselves surprisingly in the same direction as the wave propagation, unlike for planar or single helical wave propulsion. For the range of parameters explored in this paper, this direction reversal is found to occur only in the opposite-chirality configuration for sufficiently large R and r (figure 7c(ii)), while the average propagation velocity $\langle U_z \rangle$ is always negative for the same-chirality configuration (i.e. the swimming direction is always opposite to the direction of the propagating wave; figure 7c(i)). In figure 8, we show the detailed swimming velocities of two opposite-chirality superhelical swimmers, where one of them has its longitudinal propulsion in the opposite direction relative to the wave propagation ($R = 7$, $r = 0.4$; figure 8a), and the other in the same direction as the wave propagation ($R = 9$, $r = 0.4$; figure 8b). It is intriguing that a small change in the geometry (see the corresponding superhelices in figure 8a(ii),b(ii))

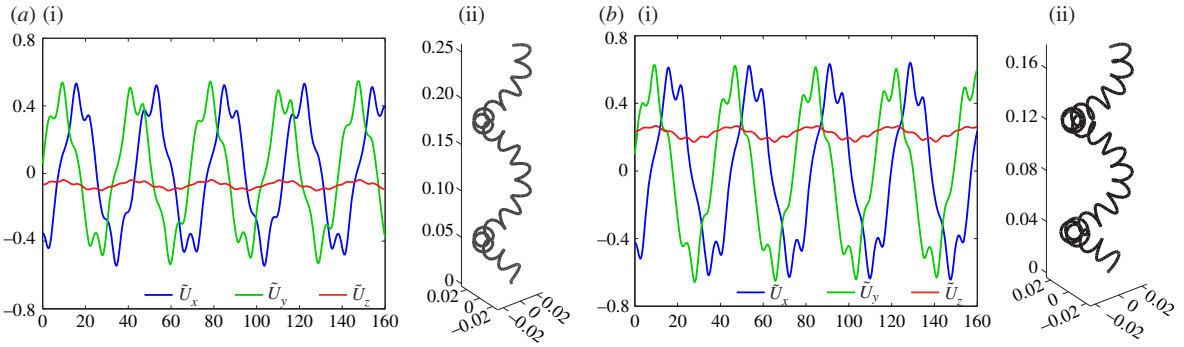

Figure 8. Three-dimensional swimming velocities in the laboratory frame (a(i), b(i)) of two opposite-chirality superhelical swimmers, and their corresponding geometries (a(ii), b(ii)). (a) $R = 7$, $r = 0.4$ and U_z is negative, while the wave propagation is towards the positive z-direction; (b) $R = 9$, $r = 0.4$ and U_z is positive, while the wave propagation is towards the positive z-direction. Geometric data of *Cu. melleus* spermatozoa are used for other parameters. (Online version in colour.)

can lead to a swimming direction reversal. We argue in the next section (§3.4) that this transition is related to the hydrodynamic interaction between distinct parts of the superhelical flagellum.

3.4. Comparison between slender body theory and resistive force theory

In order to consider the relative importance of non-local hydrodynamic interactions in the swimming of superhelices, we now compare our results with those obtained using the more commonly used local drag model (equation (2.6), but neglecting the non-local term **K**). The local drag model (so-called RFT) ignores hydrodynamic interactions between distinct parts of the curved flagellum, and is expected to work well [21–23] for simple geometries, where different parts of the body are sufficiently well separated. However, for more complicated geometries, the local drag model may not capture even the correct qualitative features. Recently, Jung *et al.* [20] studied the rotational dynamics of opposite-chirality superhelices and found a qualitative discrepancy (the rotational direction of the superhelix when being towed in a viscous flow) between the experimental results and the predictions from the RFT. Other recent works have also shown the inadequacy of the local drag model [32,37].

Figure 9 shows the swimming speeds computed with both non-local SBT and RFT using two sets of geometrical data: *Cu. melleus* (figure 9*a* (same-chirality) and figure 9*b* (opposite-chirality)), and *T. molitor* (figure 9*c* (same-chirality) and figure 9*d* (opposite-chirality)). In these two cases, all other parameters are fixed but the amplitude ratio r is varied from 0 to 0.5. Increasing r complicates the swimmer geometry, and the hydrodynamic interactions are expected to be more significant for large r. For the case of *Cu. melleus* (figure 9*a*,*b*), we see good (even quantitative) agreement between the results form the SBT (solid lines) and the RFT (dashed lines). However, for the case of *T. molitor* (figure 9*c*,*d*), which has larger values of R and K, the deviation between the two models becomes significant for the same-chirality configuration (figure 9*c*) as r increases. There are even qualitative discrepancies: in the opposite-chirality configuration (figure 9*c*) for large values of r, the RFT fails to capture the transition in the sign of $\langle U_z \rangle$ predicted by the SBT. As no such transition is found when the hydrodynamic interactions are ignored, this transition may be attributed to non-local hydrodynamic interactions of the body with itself. In general, and perhaps unsurprisingly, we have shown that the local drag model breaks down when the geometry of the structure is sufficiently intricate.

3.5. Asymptotic analysis

In the locomotion of some species of spermatozoa, the minor wave amplitude is much smaller than the major wave amplitude (tables 1 and 2), which motivates us to perform an asymptotic analysis for $r \ll 1$. Such an asymptotic analysis linearizes the problem geometrically and allows the nonlinear effects to be taken into account order by order, making the problem more amenable to mathematical analysis. However, even in the asymptotic consideration, three-dimensional force and torque balances do not yield tractable analytical results. Hence, in the spirit of Chwang & Wu [33], we perform the force and torque balances only in the longitudinal (z-) direction using the RFT, which is expected to be at least qualitatively correct in the asymptotic limit $r \ll 1$. The local force f_z and torque m_z may be expressed as:

$$f_z = c_{U_z F_z}(t,s)\, U_z + c_{\Omega_z F_z}(t,s)\boldsymbol{\Omega}_z + c_{F_z}(t,s), \qquad (3.2)$$

and

$$m_z = c_{U_z M_z}(t,s)\, U_z + c_{\Omega_z M_z}(t,s)\boldsymbol{\Omega}_z + c_{M_z}(t,s), \qquad (3.3)$$

where the coefficients are determined analytically from equation (2.6) (without the non-local operator) and the geometry of the swimmer (equations (2.12)–(2.14)). We consider regular perturbation expansions in r for every term in equations (3.2) and (3.3), and enforce the force-free and torque-free conditions order by order. A non-zero time-averaged swimming velocity enters at $O(r^2)$. The leading order mean swimming velocities for the cases of same- and opposite-chirality

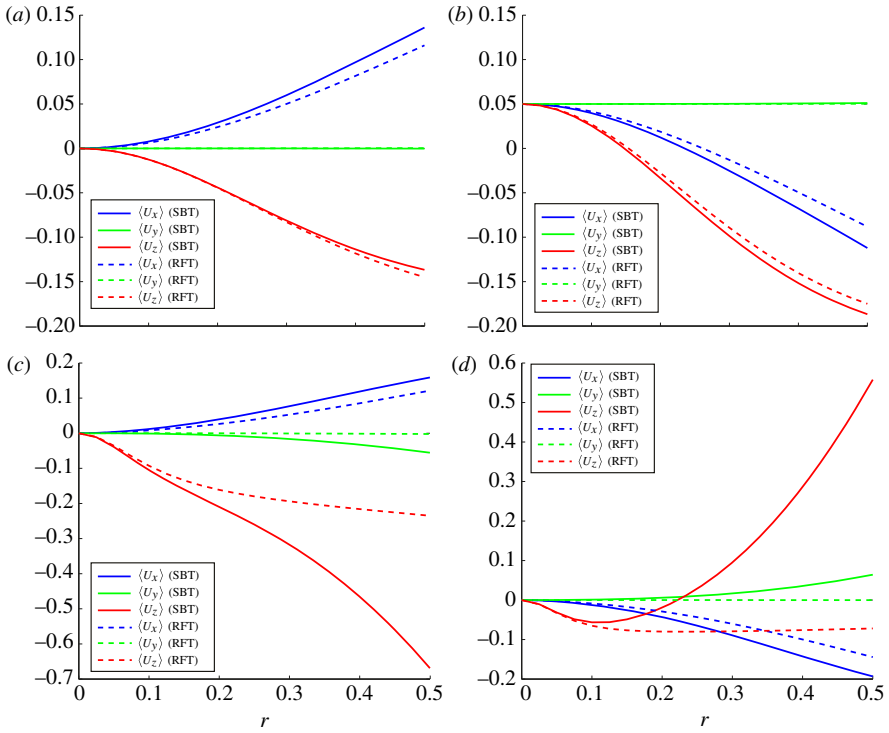

Figure 9. Comparison between the RFT (dashed lines) and the non-local SBT (solid lines) using geometric data of *Cu. melleus* spermatozoa (*a*,*b*), and *T. molitor* spermatozoa (*c*,*d*). The panels on the left (right) refer to the same- (opposite-) chirality configuration. (Online version in colour.)

configurations read

$$\tilde{U}_{\pm} \sim \frac{R^2 r^2}{2L^2(1+R^2K^2)^{3/2}} \times \{(2-2L^2)(\xi-1) + R^2K^2[2(\xi-1\pm K) - L^2(2\xi-2\pm K)] - 2[\xi-1+R^2K^2(\xi-1\pm K)]\cos L\}, \tag{3.4}$$

where $\xi = \xi_\perp/\xi_\parallel$ is the ratio of the drag coefficients in the normal direction to the longitudinal direction ($\xi_\parallel = 4\pi/c_0, \xi_\perp = 8\pi/(2+c_0)$). For very slender filaments, $\xi \approx 2$. We note that the substitution $K \rightarrow -K$ in equation (3.4) converts the same-chirality speed $\tilde{U}_+$ to the opposite-chirality speed $\tilde{U}_-$. The propulsion speed has a quadratic dependence on the minor wave amplitude for small r, which is also found in planar [38] and helical [39] geometries.

These asymptotic results (equation (3.4)) are compared with the finite-amplitude simulations (both the RFT and the SBT predictions) in figure 10, for a very small amplitude ratio of $r = 0.01$ and a slenderness ratio of $\epsilon = 1/1000$. There is excellent agreement between the asymptotic results and the finite amplitude RFT simulations. The discrepancy between the non-local SBT and the local drag model highlights the importance of non-local hydrodynamic interactions for such organisms.

We conclude by pointing out an intriguing theoretical curiosity, that drag anisotropy ($\xi \neq 1$) is not required for superhelical swimming: setting $\xi = 1$ in equation (3.4), non-zero mean propulsion velocities (of equal magnitude but opposite signs) are obtained for both chirality configurations,

$$\tilde{U}_{\pm}(\xi=1) = \mp \frac{R^4K^3(L^2-2+2\cos L)}{2L(1+R^2K^2)^{3/2}} r^2. \tag{3.5}$$

Note that Becker *et al.*'s [40] argument of the requirement of drag anisotropy for locomotion is only true for inextensible swimmers and does not apply here. The superhelical kinematics described (equations (2.12)–(2.14)) are possible only when extensibility is allowed; the minor helix is built upon another curved structure (the major helix) and local extension and contraction is implied in the wave kinematics. When extensibility is permitted, the relaxation of the drag anisotropy requirement has been recently shown [41]. That the swimming speed is non-zero is owing to intrinsic variations in length (and hence drag) embedded in the curved geometry of the superhelices. A minor helix built upon a major helix has relatively shorter lengths in the regions closer to the longitudinal axis, creating an overall imbalance of hydrodynamic drag even in the isotropic drag case ($\xi = 1$). A similar example is a toroidal helix (a helix built upon a circle), which is an idealized model studied recently for dinoflagellates [42]. We expect that the propagation of a wave along a toroidal helix should also require extensibility, and that propulsion is still possible even without drag anisotropy [41].

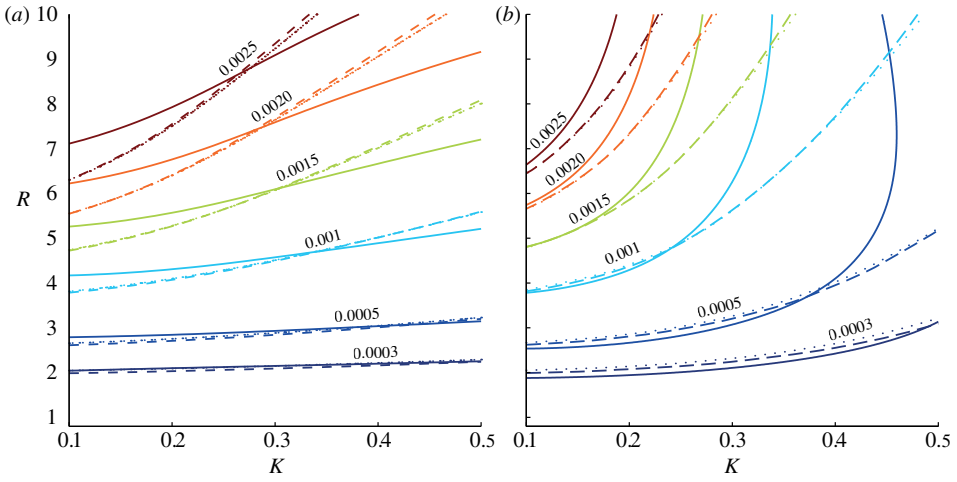

Figure 10. Comparison of the asymptotic results (dotted lines) with the finite-amplitude simulations using the RFT (dashed lines) and the non-local SBT (solid lines). Shown are the contour lines of the average swimming velocity $\bar{U}_{\pm}$ for the (*a*) same-chirality, and (*b*) opposite-chirality configurations for a small minor to major wave amplitude ratio of $r = 0.01$. (Online version in colour.)

4. DISCUSSION

In this paper, we have studied a morphologically interesting double-wave structure exhibited by various insect spermatozoa. The construction of such spermatozoa is considerably more complex than those for flagella which exhibit simpler planar or helical waves: the flagellum does not only have a more complicated $9 + 9 + 2$ arrangement of microtubules but also mitochondrial derivatives and accessory bodies running along the axoneme [5]. We have mathematically idealized the double-wave structure as a superhelical structure and presented a hydrodynamic study on superhelical swimming. The available data are primitive and sparse; nevertheless, we consider the agreement between experimental measurements and the theory explored herein to be quite reasonable. Through numerical experiments, we have found that the major wave speed has little contribution to propulsion when the sperm head is small, as is the case for insect spermatozoa. When there is no sperm head, the propulsion speed is independent of the major wave speed and depends entirely upon the minor wave speed. We have also explored the dependence of the propulsion speed on the dimensionless major wave amplitude R and the ratio of the minor to major wave amplitudes r (figure 7), and counterintuitive behaviours have been found for the opposite-chirality configuration. In particular, we have found that propulsion and wave propagation can occur in the same direction for superhelices in the opposite-chirality configuration.

The present study suggests that the major wave has negligible influence on the motility of a superhelical swimmer. This finding favours the recent hypothesis by Werner *et al.* [10] that the major helical wave is a static (non-propagating) structure; the minor wave structure is solely responsible for the motility, and the apparent major wave propagation is simply owing to the passive rotation of the entire geometry (see §1). However, in the study by Baccetti *et al.* [16] on the motility of *Ce. capitata*, they have adopted the same experimental techniques as in Gibbons *et al.* [43], which distinguished the rolling frequency from the apparent beat frequency. In their work, the rolling frequency was measured by stroboscopic observation of the eccentrically attached sperm head, and the flagellar beat frequency was measured by the same means with the sperm head adhered to the bottom of the observation dish. Using this method, the major wave speed measured should be taken as an active propagation speed. We are not in a position to provide a definite answer on whether or not the major wave propagates actively in actual insect spermatozoa. However, according to the present study, we suspect that there might be some biological reasons, other than motility, for the major wave to propagate actively. We also do not know if the propagation of the major wave is a biological prerequisite for the propagation of the minor wave. Further biological studies are required to answer these questions.

It is illuminating to compare the superhelical swimming studied here with regular helical swimming. The swimming trajectories are qualitatively different in the two cases: in regular helical swimming, the trajectory is a regular helix, whereas in superhelical swimming the trajectory is doubly helicated. In addition, a regular helical flagellum cannot swim on its own; a sperm head is required to swim (as the absence of a sperm head renders the deformation of the regular helix a rigid body motion). By contrast, the propagation of superhelical waves along a flagellum is in general not equivalent to rigid body motion, and hence 'head-less' swimming is possible. This might help explain the presence of only a small slender sperm head in insect spermatozoa. In other words, superhelical swimming can be viewed as an alternative mechanism to the regular helical swimming when only a small sperm head is available.

Finally, a non-local SBT was used in this work and compared with a simpler and widely used local drag model. We showed that the RFT failed to capture even the qualitative features of the swimmer when the

geometry becomes complicated. The results suggest that further hydrodynamic studies on superhelical structures require more advanced models than the local RFT, such as the SBT employed here. Optimization with respect to the efficiency of the swimmer taking into account the viscous dissipation, and other energy costs owing to bending and internal sliding of filaments [31], which have been neglected in this work, will be interesting for future work.

This work was funded in part by the US National Science Foundation (Grant CBET-0746285 to E.L.) and the Croucher Foundation (through a scholarship to O.S.P.). Useful conversations with Dr Michael Werner and Dr Anne Swan are gratefully acknowledged.

REFERENCES

1 Biewener, A. A. 2003 *Animal locomotion*. Oxford, UK: Oxford University Press.
2 Fauci, L. J. & Dillon, R. 2006 Biofluid mechanics of reproduction. *Annu. Rev. Fluid Mech.* **38**, 371–394. (doi:10.1146/annurev.fluid.37.061903.175725)
3 Lauga, E. & Powers, T. 2009 The hydrodynamics of swimming microorganisms. *Rep. Prog. Phys.* **72**, 096601. (doi:10.1088/0034-4885/72/9/096601)
4 Brennen, C. & Winet, H. 1977 Fluid mechanics of propulsion by cilia and flagella. *Annu. Rev. Fluid Mech.* **9**, 339–398. (doi:10.1146/annurev.fl.09.010177.002011)
5 Werner, M. & Simmons, L. W. 2008 Insect sperm motility. *Biol. Rev.* **83**, 191–208. (doi:10.1111/j.1469-185X.2008.00039.x)
6 Baccetti, B. 1972 Insect sperm cells. *Adv. Insect Physiol.* **9**, 315–397. (doi:10.1016/S0065-2806(08)60279-9)
7 Rikmenspoel, R. & Isles, C. A. 1985 Digitized precision measurements of the movements of sea urchin sperm flagella. *Biophys. J.* **47**, 395–410. (doi:10.1016/S0006-3495(85)83931-X)
8 Jamieson, B. G. M., Dallai, R. & Afzelius, B. A. 1999 *Insects: their spermatozoa and phylogeny*. Enfield, NH: Science Publishers Inc.
9 Morrow, E. H. 2004 How the sperm lost its tail: the evolution of aflagellate sperm. *Biol. Rev.* **79**, 795–814. (doi:10.1017/S1464793104006451)
10 Werner, M., Tscheulin, T., Speck, T., Zissler, D. & Peschke, K. 2002 Ultrastructure and motility pattern of the spermatozoa of *Aleochara curtula* (Coleoptera, Staphylinidae). *Arth. Struct. Dev.* **31**, 243–254. (doi:10.1016/S1467-8039(02)00046-4)
11 Baccetti, B., Burrini, A. G., Dallai, R., Giusti, F., Mazzini, M., Renieri, T., Rosati, F. & Selmi, G. 1973 Structure and function in the spermatozoon of *Tenebrio molitor* (the spermatozoon of Arthropoda. XX). *J. Mechanochem. Cell Motil.* **2**, 149–161.
12 Baccetti, B., Burrini, A. G., Dallai, R., Pallini, V., Periti, P., Piantelli, F., Rosati, F. & Selmi, G. 1973 Structure and function in the spermatozoon of *Bacilus rossius*: the spermatozoon of Arthropoda. XIX. *J. Ultrastruct. Res.* **44**, 1–73.
13 Phillips, D. M. 1974 Structural variants in invertebrate sperm flagella and their relationship to motility. In *Cilia and flagella* (ed. M. A. Sleigh), pp. 379–402, London, UK: Academic Press.
14 Linley, J. R. 1979 Activity and motility of spermatozoa of *Culicoides melleus* (Diptera: Ceratopogonidae). *Entomol. Exp. Appl.* **26**, 85–96. (doi:10.1111/j.1570-7458.1979.tb02902.x)
15 Swan, M. A. 1981 The generation and propagation of double waves in mosquito (*Aedes notoscriptus*) sperm-tails. *Gamete Res.* **4**, 241–250. (doi:10.1002/mrd.1120040308)
16 Baccetti, B., Gibbons, B. H. & Gibbons, I. R. 1989 Bidirectional swimming in spermatozoa of Tephritid flies. *J Submicrosc. Cytol. Pathol.* **21**, 619–625.
17 Bressac, C., Joly, D., Devaux, J., Serres, C., Feneus, D. & Lachaise, D. 1991 Comparative kinetics of short and long sperm in sperm dimorphic *Drosophila* species. *Cell Motil. Cytoskel.* **19**, 269–274. (doi:10.1002/cm.970190405)
18 Curtis, S. K. & Benner, D. B. 1991 Movement of spermatozoa of *Megaselia scalaris* (Diptera: Brachycera: Cyclorrhapha: Phoridae) in artificial and natural fluids. *J. Morphol.* **210**, 85–99. (doi:10.1002/jmor.1052100108)
19 Werner, M., Gack, C., Speck, T. & Peschke, K. 2007 Queue up, please! Spermathecal filling in the rove beetle *Drusilla canaliculata* (Coleoptera, Staphylinidae). *Naturwissenschaften* **94**, 837–841. (doi:10.1007/s00114-007-0257-8)
20 Jung, S., Mareck, K., Fauci, L. & Shelley, M. 2007 Rotational dynamics of a superhelix towed in a Stokes fluid. *Phys. Fluids* **19**, 103105. (doi:10.1063/1.2800287)
21 Wiggins, C. H., Riveline, D., Ott, A. & Goldstein, R. E. 1998 Trapping and wiggling: elastohydrodynamics of driven microfilaments. *Biophys. J.* **74**, 1043–1060. (doi:10.1016/S0006-3495(98)74029-9)
22 Yu, T. S., Lauga, E. & Hosoi, A. E. 2006 Experimental investigations of elastic tail propulsion at low Reynolds number. *Phys. Fluids* **18**, 091701. (doi:10.1063/1.2349585)
23 Riedel-Kruse, I. H., Hilfinger, A., Howard, J. & Julicher, F. 2007 How molecular motors shape the flagellar beat. *HFSP J.* **1**, 192–208. (doi:10.2976/1.2773861)
24 Johnson, R. E. 1980 An improved slender-body theory for stokes flow. *J. Fluid Mech.* **99**, 411–431. (doi:10.1017/S0022112080000687)
25 Atkinson, K. E. 1997 *The numerical solution of integral equations of the second kind*. Cambridge, UK: Cambridge University Press.
26 Götz, T. 2000 Interactions of fibers and flow: asymptotics, theory and numerics. PhD thesis, University of Kaiserslautern, Germany.
27 Tornberg, A. K. & Shelley, M. J. 2004 Simulating the dynamics and interactions of flexible fibers in Stokes flows. *J. Comput. Phys.* **196**, 8–40. (doi:10.1016/j.jcp.2003.10.017)
28 Lighthill, J. 1975 *Mathematical biofluid dynamics*. Philadelphia, PA: SIAM.
29 Chattopadhyay, S., Moldovan, R., Yeung, C. & Wu, X. L. 2006 Swimming efficiency of bacterium *Escherichia coli*. *Proc. Natl Acad. Sci. USA* **103**, 13 712–13 717. (doi:10.1073/pnas.0602043103)
30 Childress, S. 1981 *Mechanics of swimming and flying*. Cambridge, UK: Cambridge University Press.
31 Spagnolie, S. E. & Lauga, E. 2010 The optimal elastic flagellum. *Phys. Fluids* **22**, 031901. (doi:10.1063/1.3318497)
32 Spagnolie, S. E. & Lauga, E. 2011 Comparative hydrodynamics of bacterial polymorphism. *Phys. Rev. Lett.* **106**, 058103. (doi:10.1103/PhysRevLett.106.058103)
33 Chwang, A. T. & Wu, T. Y. 1971 A note on the helical movement of micro-organisms. *Proc. R. Soc. Lond. B* **178**, 327–346. (doi:10.1098/rspb.1971.0068)
34 Keller, J. B. & Rubinow, S. I. 1976 Swimming of flagellated microorganisms. *Biophys. J.* **16**, 151–170. (doi:10.1016/S0006-3495(76)85672-X)
35 Margulis, L., Chapman, M., Guerrero, R. & Hall, J. 2006 The last eukaryotic common ancestor (leca): acquisition of cytoskeletal motility from aerotolerant spirochetes in the proterozoic eon. *Proc. Natl Acad. Sci. USA* **103**, 13 080–13 085. (doi:10.1073/pnas.0604985103)

36 Nicastro, D., McIntosh, J. R. & Baumeister, W. 2005 3D structure of eukaryotic flagella in a quiescent state revealed by cryo-electron tomography. *Proc. Natl Acad. Sci. USA* **102**, 15 889–15 894. (doi:10.1073/pnas.0508274102)

37 Chattopadhyay, S. & Wu, X. L. 2009 The effect of long-range hydrodynamic interaction on the swimming of a single bacterium. *Biophys. J.* **96**, 2023–2028. (doi:10.1016/j.bpj.2008.11.046)

38 Taylor, G. 1951 Analysis of the swimming of microscopic organisms. *Proc. R. Soc. Lond. A* **209**, 447–461. (doi:10.1098/rspa.1951.0218)

39 Taylor, G. 1952 The action of waving cylindrical tails in propelling microscopic organisms. *Proc. R. Soc. Lond. A* **211**, 225–239. (doi:10.1098/rspa.1952.0035)

40 Becker, L. E., Koehler, S. A. & Stone, H. A. 2003 On self-propulsion of micro-machines at low Reynolds number: Purcell's three-link swimmer. *J. Fluid Mech.* **490**, 15–35. (doi:10.1017/S0022112003005184)

41 Pak, O. S. & Lauga, E. 2011 Extensibility enables locomotion under isotropic drag. *Phys. Fluids* **23**, 081702. (doi:10.1063/1.3624790)

42 Nguyen, H., Ortiz, R., Cortez, R. & Fauci, L. 2011 The action of waving cylindrical rings in a viscous fluid. *J. Fluid Mech.* **671**, 574–586. (doi:10.1017/S0022112010006075)

43 Gibbons, B. H., Baccetti, B. & Gibbons, I. R. 1985 Live and reactivated motility in the 9+0 flagellum of *Anguilla* sperm. *Cell Motil.* **5**, 333–350. (doi:10.1002/cm.970050406)